Synchrotron X-ray imaging via ultra-small angle scattering, principles of quantitative analysis and application in studying bone integration to synthetic grafting materials

Sérgio L. Morelhão,[1,*] Paulo G. Coelho,[2] and Marcelo G. Hönnicke[3]

[1]*Instituto de Física, Universidade de São Paulo, São Paulo, SP, Brazil*
[2]*Department of Biomaterials and Biomimetics, New York University, NY, USA*
[3]*NSLS II, Brookhaven National Laboratory, 11973, Upton NY, USA.*

(Dated: April 4, 2009)

Optimized experimental conditions for extracting accurate information on sub-pixel length scales from analyzer based X-ray imaging were obtained and applied to investigate bone regeneration by means of a synthetic β-TCP grafting materials in a rat calvaria model. The results showed a 30% growth in the particulate size due to bone ongrowth/ingrowth within the critical size defect over one month healing period.

PACS numbers: 87.59.-e, 87.85.J-

Phase contrast X-ray imaging[1–4] is a well-established tool to evidence details of biological tissues that are invisible or indistinguishable by conventional radiography. Its applications have been evaluated in many scientific fields and with a variety of phase sensitive techniques.[5–7] Analyzer-based imaging (ABI)[2,8] is sensitive to the phase gradient due to refraction. However, differently from the other techniques, ABI is also capable of providing information on two other major radiation-matter interaction processes: photoelectric absorption and small-angle scattering.[9] Although refraction is the contrast mechanism able to resolve features on the length scale of the spatial resolution of detector systems, typically of the order of some tens of microns, small-angle scattering is the process sensitive to density fluctuation on shorter scales, of a few microns or less. Extensively exploited to probe low ordered systems, such as macro molecules in solution, small-angle scattering techniques are one of the most fundament X-ray tools for the microstructure characterization of solid and fluid materials.[10] In despite of its short-scale probing potential, small-angle scattering as an imaging contrast mechanism, where it is commonly called ultra-small-angle X-ray scattering (USAXS), has been treated marginally, qualitatively in a few cases[6,11] but, in most cases, as a sub-product owing to a non-desired process that can smear fine structural details of the refraction images.[12–15] In medicine, biology, and related fields, the usage of USAXS images to localize and characterize distinct distributions of microscopic alterations over vast pathological tissues (centimeter scale) opens terrific opportunities in studying multifactorial diseases with large ensembles of clinical cases, as for instance in the study of cataract.[6] To achieve its full potential as a general imaging process, it is fundamental to develop data analysis procedures able to determine the accuracy by which the length scale of the density fluctuation on a sub-pixel resolution can be retrieved from the USAXS images. In this work, one of such procedures is developed. It shows how drastically accuracy depends on experimental ABI setups. It also leads to optimized conditions for specific applications, as demonstrated here in the study of bone integration to biocompatible materials, which is also an important subject.

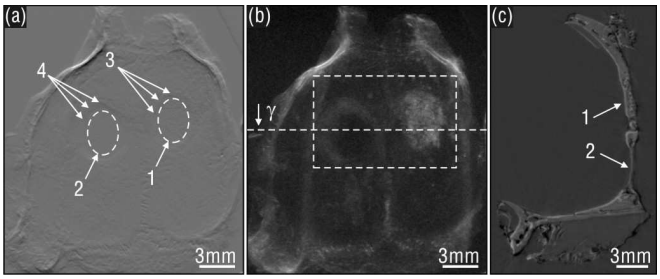

FIG. 1: (a,b) Multiple image radiography of rat calvaria: (a) refraction image; and (b) differential absorption (scattering) image. CP and blood clot filled defects are denoted by dashed circles, arrows 1 and 2, respectively. CP-bone integration zone (IZ), e.g. arrows 3, and zone of thick naturally grown bone (NGB) since surgery, e.g. arrows 4, are visible. (c) Two-dimensional computer tomography processed at position γ, dashed-line in (b), and analyzer setting at the slope of its RC. 1: CP filled; 2: thin NGB. Experimental setup: A111E52.

Form and function replacement of lost hard tissue through guided regeneration with either synthetic materials or tissue engineering (tissue regeneration at cellular level) has been of interest of both healthcare practitioners and patients. The reason for such interest include the avoidance of a second surgical site and procedure, i.e. autologous bone grafting, and the potential secondary infection due to cadaveric (allogenous) and animal (xenogenous) bone processing for grafting purposes.[16,17] Among bioceramics, Ca- and P-based synthetic materials such as hydroxyapatite, β-tricalcium phosphate (β-TCP), or $Ca_3(PO_4)_2$, and biphasic blends have been widely utilized in dentistry and orthopedics.[16] These materials have been employed as bone defect filling materials, implant coatings, bone substitutes, drug delivery/biologic carriers, and resorbable scaffolds.[17] These various applications originated due to their degradation followed by bone replacement as time elapses in vivo.[16,17] Here, artificial bone regeneration by means of a synthetic

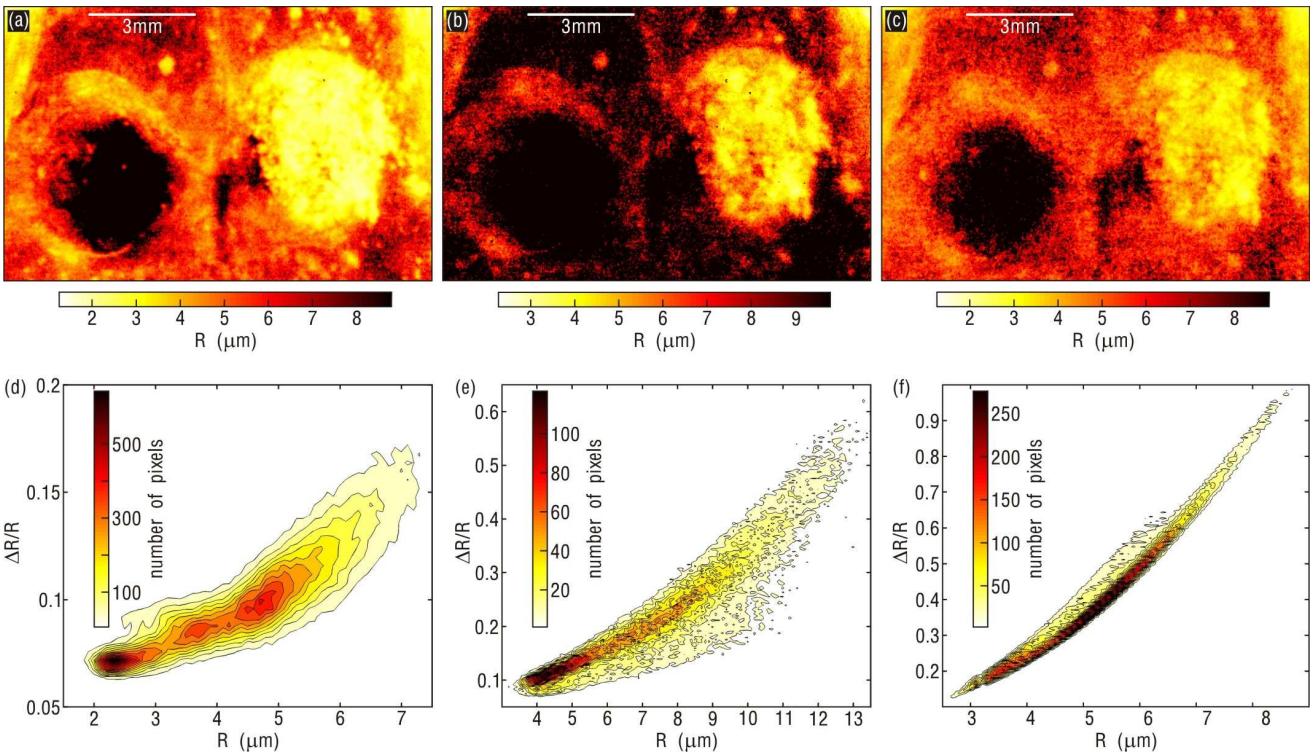

FIG. 2: (a,b,c) R images and (d,e,f) their respective accuracy, $\Delta R/R$, for three experimental setups: (a,d) A333E30; (b,e) A333E52; and (c,f) A111E52. Sample #1, imaged area of 257×401 pixels [Fig. 1(b)].

β-TCP grafting materials in a rat calvaria model was investigated by spatially resolved USAXS images.

Any scattering process is characterized by a reciprocal law, which gives an inverse relationship between particle size and scattering angle.[10] For electron density inhomogeneities on a length scale R, this law also applies, providing that the angular spreading of the scattered radiation, of wavelength λ, is roughly proportional to λ/R. In more specific terms, a statistical intensity distribution $\Gamma(\Delta\theta)$ can be assigned to each particular kind of inhomogeneity to describe the process as a function of the scattering angle $\Delta\theta$ from the incident beam direction. The angular spreading on a given scattering plane can hence be characterized by the quantity

$$\sigma_{\rm u}^2 = \int_{-\alpha}^{+\alpha} (\Delta\theta)^2\, \Gamma(\Delta\theta)\, {\rm d}\Delta\theta = \left[\frac{\lambda C_\Gamma(\alpha)}{R}\right]^2 , \qquad (1)$$

which is the standard deviation of the statistical distribution. $C_\Gamma(\alpha)$ is constant for non-truncated integrals, i.e. when $\alpha >> \sigma_{\rm u}$. From the general theory of small-angle scattering of X-rays, it is well known that the central region of the scattering curves is quite irrespective to the shape and symmetry of the scattering centers as long as they have the same radius of gyration R_g, as usually obtained from Guinier Law in a conventional SAXS experiment.[10] Since $\sigma_{\rm u}$ is also essentially determined by the central region of the curves, its value is practically independent of $\Gamma(\Delta\theta)$, except for very anisometric scattering centers such as with pronounced disc- or rod-like shapes. Then, within the Guinier approximation of the scattering curves $\Gamma(\Delta\theta) = a\pi^{-1/2}\, \exp(-a^2\Delta\theta^2)$ where $a = 2\pi R_g/\lambda\sqrt{3}$, which provides $\sigma_{\rm u} = \lambda\sqrt{1.5}/2\pi R_g$. To quantify the size of the scattering centers, i.e. the length scale of sub-pixel density fluctuation in the samples, we have used the average spherical radius $R = R_g\sqrt{5/3}$, instead of R_g, and hence $C_\Gamma \cong 1/4$ in Eq. (1).

Typical ABI setups require a parallel monochromatic beam and an analyzer crystal placed between the sample and the imaging detector. Under the condition that photons exiting the object plane at a given point are scattered in the vertical plane, i.e. the diffraction plane of the analyzer crystal, according to $\Gamma(\Delta\theta)$ and that each pixel in the detector is collecting all such photons,[15] the USAXS images are composed by the values of $\sigma_{\rm u}$ as given in Eq. (1). In the statistical algorithm used to process multiple images from ABI data,[14] two rocking curves (RCs) of the analyzer crystal have to be recorded on each pixel: one with the sample, the *object* RC, and another without the sample, the *reference* RC. Any difference in the standard deviations $\sigma_{\rm obj}$ and $\sigma_{\rm ref}$ of these RCs is directly related to the amount of USAXS on a given pixel since $\sigma_{\rm u} = (\sigma_{\rm obj}^2 - \sigma_{\rm ref}^2)^{1/2}$, as detailed in Ref. 14. The reciprocal law summarized in Eq. (1) is used here to determine the accuracy

TABLE I: Details of the experimental ABI setups: analyzer $hk\ell$ Bragg reflection, X-ray energy E, experimental ($W_{\rm E}$) and theoretical[12] ($W_{\rm T}$) FWHM of the RC, angular range $2w$ centered in the RC for image acquisition in increments of $\mathrm{d}\theta$, and average maximum number of counts per pixel $\langle N_{\rm m}\rangle$ acquired during the *reference* RC.

Setup (label)	$hk\ell$	E (keV)	$W_{\rm E}/W_{\rm T}$ (μrad)	w (μrad)	$\mathrm{d}\theta$ (μrad)	$\langle N_{\rm m}\rangle$ (counts)
A333E30	333	30	1.9/2.10	15	0.5	14856
A333E52	333	52	1.3/1.29	8	0.4	11545
A111E52	111	52	6.3/6.30	20	1.0	31498

$$\Delta R/R = 8(R/\lambda)^2\sqrt{[\Delta(\sigma^2_{\rm obj})]^2 + [\Delta(\sigma^2_{\rm ref})]^2} \qquad (2)$$

by which sub-pixel density fluctuations are resolved. It is given in terms of the errors $\Delta(\sigma^2_{\rm obj})$ and $\Delta(\sigma^2_{\rm ref})$ in the square values of the standard deviations. Both errors estimated by propagating in the equations of $\sigma^2_{\rm obj}$ and $\sigma^2_{\rm ref}$ the statistical noise, $\pm\sqrt{N(\theta_n)}$, of radiation counting in the RCs where $N(\theta_n)$ is the number of counts in a pixel for the angular setting θ_n of the analyzer crystal.

X-ray measurements were performed at station X15A of the synchrotron light source (NSLS) in the Brookhaven National Laboratory. The two-bounce Si (111) monochromator of the beamline has been set to non-dispersive configuration with the analyzer Si (111) crystal in all the used experimental setups, whose details are summarized in Table I. Pixel size of the imaging detector system is 30 μm. Samples were prepared by surgery, which consisted of creating two 4 mm diameter defects in the rat calvaria. One defect was filled with synthetic β-TCP grafting material (Synthograft$^{\rm TM}$, Bicon LLC, Boston, USA) and the other was left filled with the blood clot (control). The rats were sacrificed at 4 weeks after surgery, and the samples were maintained in 70 % ethanol until tested.

General aspects of the samples are depicted via the refraction image of sample #1 that is shown in Fig. 1(a): CP filled defect, control defect, CP-bone integration zone (IZ), and zone of naturally grown bone (NGB) since surgery. Scattering centers in the region of interest, embracing both defects, are evidenced by processing a differential absorption image,[14] Fig. 1(b). Besides an enhanced scattering at the CP filled defect, scattering at the NGB zone can also be clearly observed. A computed tomography slice of the sample, Fig. 1(c), provides information on the actual thickness of both defects. The sub-pixel spatial resolution is investigated in two steps: *i)* R images processed from ordinary USAXS images by using the relationship $R = 0.25\lambda/\sigma_{\rm u}$, Eq. (1); and *ii)* graphical analysis of the distribution of $\Delta R/R$ as a function of R, Eq. (2). In Fig. 2, the results of such investigation on the selected area in Fig. 1(b) and for the three ABI setups in Table I are shown. Similar evaluation on the CP

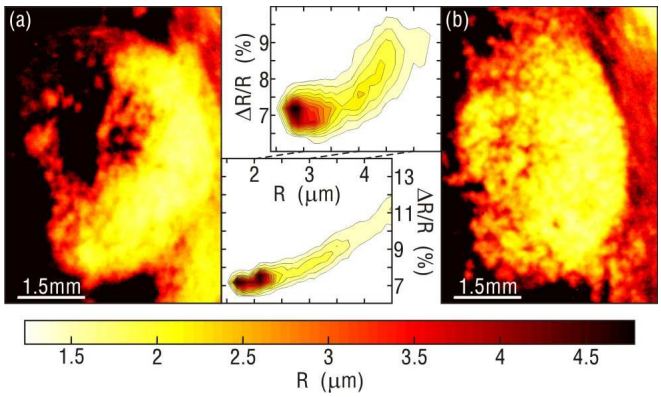

FIG. 3: R images on CP filled defects on (a) sample #2 and (b) sample #3. Radius accuracy distribution maps are given aside each corresponding image. Experimental setup: A333E30.

filled defects were also carried out on other samples, e.g. Fig. 3, but only for the A333E30 setup. It is the setup providing higher definition of specific regions of the samples, for instance the NGB interface with the original calvaria bone as seen in Fig. 2(a), as well as resolved R values, as in Fig. 2(d). Due to the limited range $2w$ of the RCs, systematic errors arise into small values of R. We provided some correction by computing $C_\Gamma(\alpha = w)$ through Eq. (1) within the spherical particle approximation for $\Gamma(\Delta\theta)$. Without any correction, the discrepancy on the minimum observed R values in the A333E52 and A111E52 setups, regarding the A333E30 one, would be more pronounced. As general results for all samples, the texture (or roughness) of the original calvaria bone provides R's of about 4.5 to 5.0 μm. In the NGB zone it decreases to 3.8 μm, and in the thin NGB region its is undetectable, Figs. 2(a) and 2(d). At the CP filled defects two distribution of particle size (radius) are identified, at $R = 1.8\,\mu$m and 2.2 μm. In most cases, both sizes can be observed, Fig. 3, as well as the occurrence of even smaller sizes ($R < 1.5\,\mu$m) on a few pixels at the central area of the grafted material [white spots in Figs. 2(a), 3(a), and 3(b)]. A granular aspect of the β-TCP grafting materials, of the order of 0.1 mm in diameter, can also be noted. But, the granules scatter as compact aggregates of tiny grains with diameter ranging from $2R \simeq 2$ to 3 μm (white spots) to about $2R = 4.0 \pm 0.4\,\mu$m almost uniformly over the rest of grafted area. This grain size gradient across the filled defects can be an evidence that the substance responsible for the thin NGB in the control defect is able to penetrate into the β-TCP granules, wrapping the tiny grains and promoting their growth by more than 1 μm in diameter during the first month after surgery.

In conclusion, within appropriated experimental conditions it has been possible to map over the extent of the imaged areas sub-pixel inhomogeneities (scattering centers) with an accuracy of about $\pm 0.2\,\mu$m, which is more than 100 times smaller than the used pixel size. The extracted information on each pixel is equivalent to

the radius of gyration obtained via SAXS experiments with microbeam of the size of the pixel. Analysis of accuracy, such as the one provided by $\Delta R/R$ [Eq. (2)], is strictly necessary to optimize the ABI setup and to extract quantitative information in studies intended to monitore changes in the size of the scattering centers. As for instance, in the study presented here where we were able to evidence gradients in the bone ingrowth process over the extent of β-TCP filled defects.

* morelhao@if.usp.br

[1] W. Wilkins, T. E. Gureyev, D. Gao, A. Pogany, and A. Stevenson, Nature **384**, 335 (1996).

[2] T. J. Davis, D. Gao, T. E. Gureyev, A. W. Stevenson, and S. W. Wilkins, Nature **373**, 595 (1995).

[3] F. Pfeifer, T. Weitkamp, O. Bunk, and C. David, Nat. Phys. **2**, 258 (2006).

[4] M. G. Hönnicke, E. M. Kakuno, G. Kellerman, I. Mazzaro, D. Abler, and C. Cusatis, Optics Express **16**, 9284 (2008).

[5] M. W. Westneat, O. Betz, R. W. Blob, K. Fezzaa, W. J. Cooper, and W.-K. Lee, Science **299**, 558 (2003).

[6] A. Antunes, A. M. V. Safatle, P. S. M. Barros, and S. L. Morelhão, Med. Phys. **33**, 2338 (2006).

[7] A. Wagner, A. Sachse, M. Keller, M. Aurich, W.-D. Wetzel, P. Hortschansky, K. Schmuck, M. Lohmann, B. Reime, J. Metge, et al., Med. Phys. Biol. **51**, 1313 (2006).

[8] E. Foerster, K. Goetz, and P. Zaumseil, Krist. Tech. **15**, 937 (1980).

[9] U. Bonse and M. Hart, Z. Physics **189**, 151 (1966).

[10] O. Glatter and O. Kratky, eds., *Small Angle Scattering of X-rays* (Academic Press, 1982).

[11] L. Levine and G. G. Long, J. Appl. Cryst. **37**, 757 (2004).

[12] Z. Zhong, W. Thomlinson, D. Chapman, and D. Sayers, Nucl. Instrum. Meth. A **450**, 556 (2000).

[13] E. D. Pisano, R. E. Johnston, D. Chapman, J. Geradts, M. V. Iacocca, C. A. Livasy, D. B. Washburn, D. E. Sayers, Z. Zhong, M. Z. Kiss, et al., Radiology **214**, 895 (2000).

[14] E. Pagot, P. Cloetens, S. Fiedler, A. Bravin, P. Coan, J. Baruchel, J. Hartwig, and W. Thomlinson, Appl. Phys. Lett. **82**, 3421 (2003).

[15] L. Rigon, F. Arfelli, and R.-H. Menk, Appl. Phys. Lett. **90**, 114102 (2007).

[16] R. Z. LeGeros, in *Monographs in Oral Science* (1991), vol. 15.

[17] J. E. Lemons, Bone **19**, S121 (1996).